TOPOLOGICAL OPTICS

Non-Hermitian topological light steering

Han Zhao[1], Xingdu Qiao[2], Tianwei Wu[2], Bikashkali Midya[2], Stefano Longhi[3], Liang Feng[2,1]*

Photonic topological insulators provide a route for disorder-immune light transport, which holds promise for practical applications. Flexible reconfiguration of topological light pathways can enable high-density photonics routing, thus sustaining the growing demand for data capacity. By strategically interfacing non-Hermitian and topological physics, we demonstrate arbitrary, robust light steering in reconfigurable non-Hermitian junctions, in which chiral topological states can propagate at an interface of the gain and loss domains. Our non-Hermitian–controlled topological state can enable the dynamic control of robust transmission links of light inside the bulk, fully using the entire footprint of a photonic topological insulator.

Controlling the flow of light on demand is critical for the next generation of photonic integrated infrastructure to sustain the ever-expanding information explosion for data processing, communication, and computing. Nevertheless, state-of-the-art integrated transmission links to efficiently guide and route light suffer two fundamental challenges: crosstalk and disorder-induced scattering losses. Most current photonic switches and routers are based on cascaded Mach-Zehnder interferometers. With complex architectures that contain numerous crossing nodes, such designs lack flexibility, require a large footprint, and thus become vulnerable to defects and scattering losses, which make large-scale integrated photonic applications impractical (*1*, *2*).

Topological photonics is revolutionizing the design principles of photonic components that benefit from these challenges by topological protection and enable robust light transport (*3*–*18*). Photonic topological insulators are synthetic materials with a gapped bulk energy spectrum and protected in-gap chiral states appearing at the edge of the structure. Topological insulating phases are characterized by an integer topological invariant that has a global dependence on characteristic parameters of the system. If the topological invariant changes across an interface separating two materials, a topological state bound to the interface necessarily occurs, providing an energy-efficient one-way channel for electromagnetic transport. These one-way channels are topologically protected such that any defect and disorder cannot induce backscattering or transmission loss, enabling photonic components with topological protection ranging from waveguiding (*4*–*11*), resonance (*12*), and lasing (*13*–*15*) in the classical regime to robust generation and propagation of single photons for quantum information (*16*–*18*).

Although topological photonics provides a solid foundation to efficiently guide, switch, and route light in integrated circuits, topological protection and reconfigurability will need to be combined for the next generation of integrated devices. Recent efforts have been devoted to the study of switching the topological phase for optical modulation (*19*–*22*), and some progress has been achieved in the microwave regime via mechanically controlled topological phase transition (*23*). However, an effective synergy between topological guiding and ultraflexible reconfigurability remains a challenge in optics. The redefinition of topological light pathways requires considerable perturbations to drive the topological phase transition inside the bulk structure, which is difficult to access in integrated photonic chips. Such a severe limitation prevents topological photonics from being practically applied, because the topological mode exists only at the static structural boundary so that most of the footprint of the photonic structure is unused.

Rather than perturbing topological robustness, we demonstrate the creation of a topological light-transport channel via non-Hermitian control on an active photonic platform within the bulk of an otherwise Hermitian photonic topological insulator with uniform topological property (Fig. 1). The topological lattice consists of coupled microring resonators supporting two topological nontrivial bandgaps (*5*) on an InGaAsP multiple–quantum well platform for operation in the telecommunication band. Non-Hermitian control is conducted by optically pumping the photonic lattice to create distributed gain (via external pumping) and loss (intrinsic material loss without pumping) domains (Fig. 1A). The emergence of new topological states is observed at the boundary of the gain and loss domains when the local non-Hermiticity (i.e., the gain–loss contrast) is driven across the exceptional point (EP) defined by the coalescing eigenstates (*24*–*29*). The associated phase transition induces two effectively detached topological states. Of these, one becomes strongly attenuated in the loss domain, whereas the other (of the gain domain) survives and enables new topological pathways for guiding light at the gain–loss domain boundary without altering the global topological properties of the photonic lattice. Therefore, non-Hermitian control can be used to actively steer topological light on demand by projecting the designed spatial pumping patterns onto the photonic lattice (Fig. 1B). Consequently, guided light can be directed along any arbitrary pathway, fully using the entire footprint in topologically routing the optical signal to any desired output port.

We consider a non-Hermitian version of the two-dimensional (2D) photonic topological microring array (*5*) consisting of a square lattice of site rings coupled via anti-resonant link rings (Fig. 1A). In the Hermitian limit, the topological insulating nature is engineered by the encircling phase $\varphi = \pi/2$, which emulates the spin-dependent magnetic flux threading a 2D electron gas. The nontrivial phase opens bandgaps where the interior structure is insulating due to destructive interference, whereas the pseudospin-dependent one-way edge-transport channels are protected. When each microring is with either gain or loss, the Hamiltonian in the pseudospin subspace is (*30*)

$$H_{1,2}^{\uparrow\downarrow} = -t\sum_{m,n}\left(a_{m+1,n}^{\dagger}a_{m,n} + e^{im\phi_{\uparrow\downarrow}}a_{m,n+1}^{\dagger}a_{m,n} + h.c.\right) - i\gamma_{1,2}a_{m,n}^{\dagger}a_{m,n}$$

where t is the coupling between two site rings controlled by the ring-to-ring separation, (m, n) labels the lattice sites in the (x, y) direction, $a(a^{\dagger})$ is the bosonic creation (annihilation) operator in the lattice site, $\phi_{\uparrow\downarrow} = \pm\varphi$ is the pseudospin-dependent encircling phase, *h.c.* denotes the Hermitian conjugate, and γ_1 (>0) and γ_2 (<0) denote the gain and loss coefficients, respectively. The topological property of the system is not altered with uniform linear gain or loss, and therefore any states in the interior are prohibited in the bandgaps. However, with a non-Hermitian gain–loss junction, imbalanced field amplitude is produced between the light circulating across the two domains, leading to the breakdown of destructive interference at the interfacial site rings. With a moderate gain–loss contrast, defined as $\Delta\gamma = \gamma_1 - \gamma_2$, a pair of "pseudo" interface states emerge in each bandgap (Fig. 2A). These counterpropagating edge states strongly couple before the closure of the bandgap and therefore are not topologically protected. By increasing the gain–loss contrast, the gap between the emerging states diminishes once they cross at the symmetry point in the reciprocal space, where the two eigenstates coalesce to one singularity (i.e., EP) (Fig. 2B). Further tuning the gain–loss contrast across the EP leads to a non-Hermitian phase transition where two newly emerged gapless interface states decouple with

[1]Department of Electrical and Systems Engineering, University of Pennsylvania, Philadelphia, PA 19104, USA. [2]Department of Materials Science and Engineering, University of Pennsylvania, Philadelphia, PA 19104, USA. [3]Dipartimento di Fisica, Politecnico di Milano and Istituto di Fotonica e Nanotecnologie del Consiglio Nazionale delle Ricerche, Piazza L. da Vinci 32, Milano I-20133, Italy.
*Corresponding author. Email: fenglia@seas.upenn.edu

each other, becoming topologically chiral and carrying two different pseudospins (Fig. 2C). The new topological interface state emerges via non-Hermitian control, which is biased to the gain domain and dominant over that on the loss side. With a large value of $\Delta\gamma/t$ (such as >5 in our study, sufficiently above the EP), the non-Hermitian chiral state possesses nearly the same modal characteristics as the original topological edge state, leading to efficient coupling between them when the pathway turns from the edge into the bulk of the lattice (*30*).

The photonic topological lattice (Fig. 3A) was fabricated on the InGaAsP multiple–quantum well platform by using electron beam lithography (*30*). We intentionally implemented shallow nanoholes on top of site rings (Fig. 3B) to sample the in-plane circulation of guided light in the far field. A uniform 200-nm edge-to-edge separation between the site rings and their adjacent link rings (Fig. 3C) opens two 70-GHz-wide bandgaps (Fig. 2, A and C). Part of the photonic topological lattice was optically pumped and can be flexibly patterned to form any arbitrary topological pathway inside the bulk of the lattice via a spatial light modulator (SLM) (*30*). The intensity of the pumping beam was precisely tuned just below the lasing threshold, offering a sufficient gain–loss contrast at the boundary of the pumping area to form the chiral non-Hermitian topological interface state while avoiding nonlinear gain saturation in each ring. To validate the new topological route along the non-Hermitian heterojunction, a uniform square pattern was created that marginally covers a 5-by-5 subarea of site rings (Fig. 3D). Owing to the intrinsic amplification nature, another advantage of our InGaAsP platform is that each site ring can also act as an on-chip light source, feeding light into the topological lattice. To make full use of this advantage, the light wave to probe the non-Hermitian–controlled topological edge states was launched from the periphery site ring next to the square pumping area, with a separate synchronized pumping beam above lasing threshold (*30*). Owing to the time-reversal symmetry of a single ring, both clockwise and counterclockwise modes lase in the site ring. Because the two modes correspond to two pseudospins of the topological lattice, they couple along the two edges of the pumping region according to their synthetic magnetic fields, respectively, topologically turning around the pump-defined (instead of structural) corners without any scattering loss (Fig. 3, E and F). The existence of the edge states is guaranteed by the topological protection, despite imperfect fabrication leading to slight discrepancy between simulations and experiments.

The virtue of the non-Hermitian–controlled topological light path is the convenient reconfiguration along any arbitrary shape to steer topological light within the entire footprint of the lattice. To demonstrate such versatile topological light steering, the pumping pattern was switched from a square shape to an L shape (Fig. 4, A to C), enabling the input beam propagation along the newly formed topological domain boundaries despite the increase of turning corners in the reconfigured pumping area. Our non-Hermitian–controlled reconfigurable light-transport scheme is inherently of topological robustness against defects. Even though a defect is intentionally created along the structural edge by a notched square pumping pattern (Fig. 4, D to F), the incident light detours around the defect ring without noticeable intensity drop and back reflection. Furthermore, because the pumping can locate the transport channel anywhere in the bulk, the light signal is allowed to take place at any site ring and be topologically guided. Such a feature was demonstrated by moving the excitation to an interior site ring (Fig. 4, G and H), where the generated lasing beam was coupled with the topological states and guided along the pumping-defined perimeters. This is in stark contrast to the prior passive photonic topological insulators, in which the topological edge states can only be accessed when probed from the edge, owing to the insulating bulk.

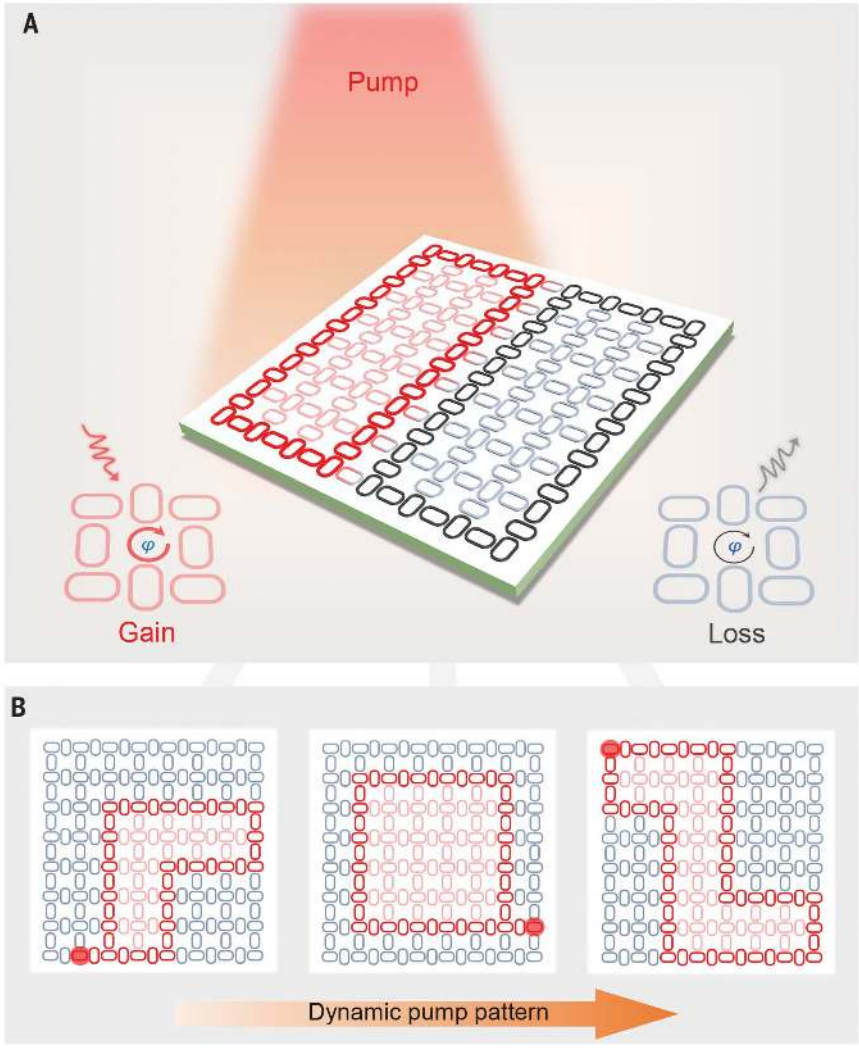

Fig. 1. Non-Hermitian control of light propagation in a topological microring lattice. (**A**) Scheme of the pump-induced local non-Hermitian symmetry breaking, which creates new topological edge channels along the gain–loss interface in the bulk of the photonic lattice with uniform global topology defined by the same geometric phase φ in the gain (red) and loss (black) plaquettes. (**B**) Topological edge states can be dynamically reconfigured to steer light along any boundaries defined by the arbitrarily patterned pump beam.

We have demonstrated active topological light steering along any arbitrary route in a photonic integrated circuit via non-Hermitian control of patterned gain–loss distribution. The non-Hermitian manipulation redefines the topological domain wall without altering the topological order of the structure, which would be otherwise static. The ultraflexible nature of non-Hermitian topological light control is general and applies to other photonic topological insulators with the size of the unit cell at the wavelength scale (*9*, *13*, *16*).

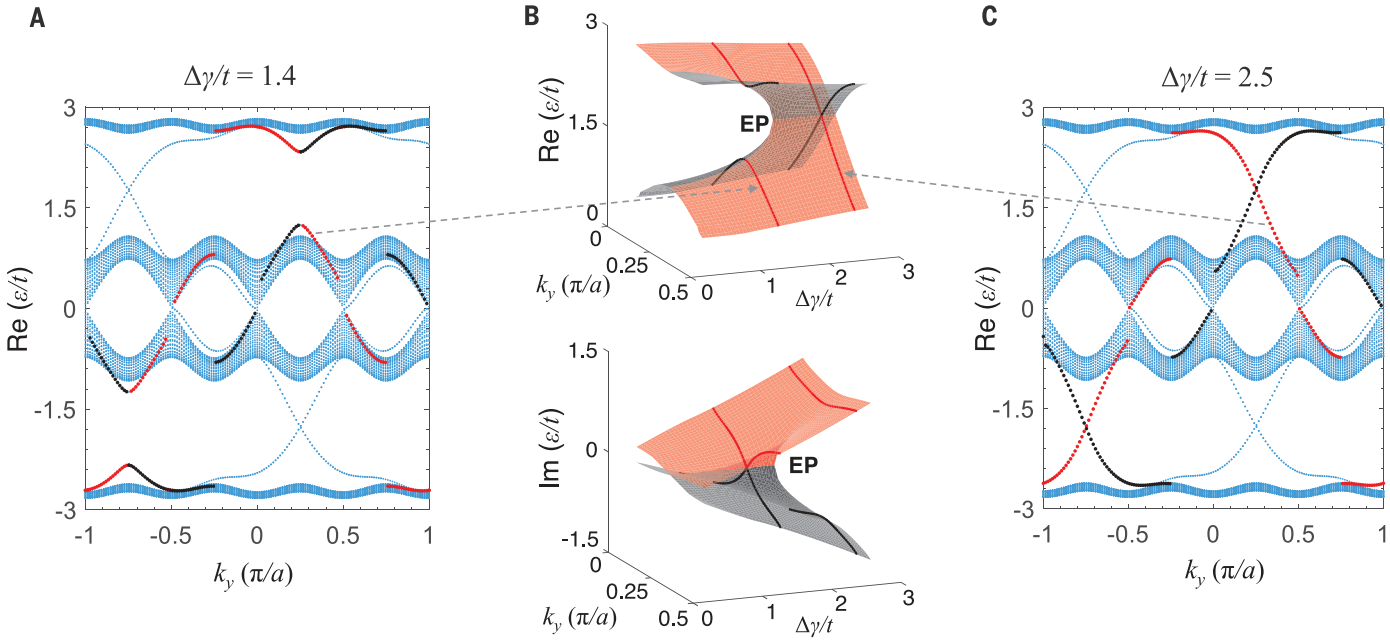

Fig. 2. Emergence of a topological interface state via a non-Hermitian phase transition. (**A**) Band structure for $\Delta\gamma = (\gamma_1 - \gamma_2) = 1.4t$ and $\varphi = \pi/2$. In addition to the edge states at the right and left physical boundaries (blue curves in the gaps), the emergence of two dispersive pseudo edge states from the bulk bands is shown near the EP degeneracies at $k_y = 0.25\pi/a$ (upper band gap) and $k_y = -0.75\pi/a$ (lower band gap). These two states are highlighted in red and black, respectively. (**B**) Riemann sheets of the real (Re) and imaginary (Im) parts of the eigenspectrum, with varying gain–loss contrast and momentum, near the EP degeneracy at ($k_y = 0.25\pi/a$, $\Delta\gamma = 1.785t$, $\gamma_1 = -\gamma_2$) in the upper bandgap. (**C**) Band structure for $\Delta\gamma = 2.5t$ showing two new anti-crossing interface states that counterpropagate at the gain–loss boundary of the lattice. The state represented by the red curve becomes amplified, whereas the state denoted by the black curve becomes strongly attenuated during propagation. ε denotes the eigenenergy.

Fig. 3. Experimental realization of the pump-defined topological states. (**A**) Scanning electron microscopy (SEM) image of the photonic topological insulator on the InGaAsP platform with an eight-by-eight area of site rings (before transfer to a glass substrate). (**B**) Zoom-in SEM image showing the shallow scattering holes of 100 nm in diameter. (**C**) Side view of a pair of coupled link and site rings, each with a cross section of 200-nm height and 500-nm width. (**D**) Uniform square pump pattern formed by a SLM that covers the five-by-five subarea of site rings (orange area) and the synchronized pump beam that induces the lasing incidence (red dot). (**E**) Simulated field amplitude distribution. White arrows show the corresponding clockwise (CW) and counterclockwise (CCW) propagation directions. (**F**) Experimentally measured field amplitude at the lasing wavelength of 1486 nm. Each plotted cylinder represents the corresponding site ring in the fabricated array.

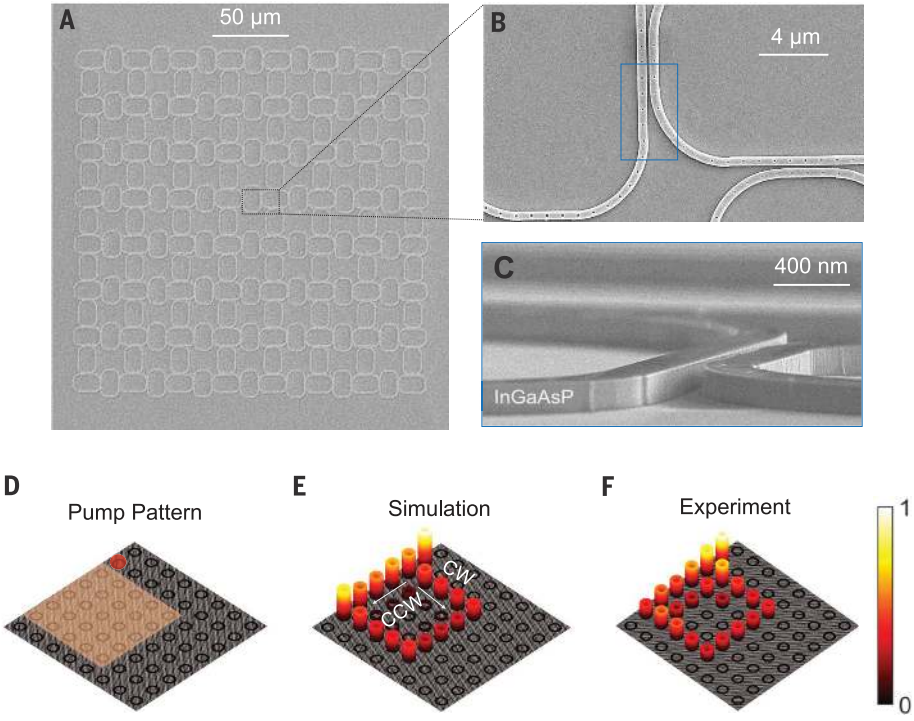

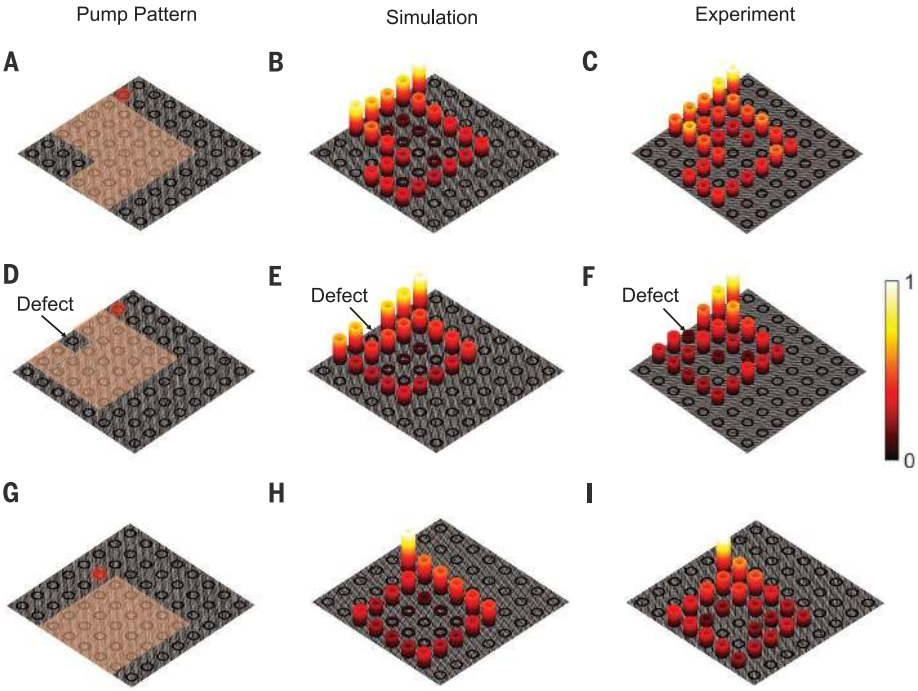

Fig. 4. Demonstration of the arbitrarily reconfigurable topological light channels. (**A**) SLM-switched L-shape pump pattern showing the reconfigurability of the gain–loss profile. (**B**) Simulated field amplitude distribution. (**C**) Experimentally measured field amplitude, revealing the reconfigured topological light path along the on-demand shape. (**D**) Notched square pump pattern that leaves a periphery site ring passive and creates a defect. (**E**) Simulated light propagation that turns around the induced defect along the non-Hermitian defined boundary. (**F**) Experimentally observed robust routing effect in the presence of the defect. (**G**) Bulk excitation by pumping the interior site ring. (**H**) Simulated field distribution with the interior incidence. (**I**) Experimentally observed topological light transport with the interior incidence.

The achievable functions can cover a variety of photonic components and networks beyond light steering and routing, thereby holding promise for the development of integrated photonic circuitry for high-density data processing.

REFERENCES AND NOTES

1. W. Dally, B. Towles, *Principles and Practices of Interconnection Networks* (Elsevier, 2004).
2. F. Testa, L. Pavesi, *Optical Switching in Next Generation Data Centers* (Springer, 2016).
3. T. Ozawa *et al*., *Rev. Mod. Phys.* **91**, 015006 (2019).
4. M. Hafezi, E. A. Demler, M. D. Lukin, J. M. Taylor, *Nat. Phys.* **7**, 907–912 (2011).
5. M. Hafezi, S. Mittal, J. Fan, A. Migdall, J. M. Taylor, *Nat. Photonics* **7**, 1001–1005 (2013).
6. M. C. Rechtsman *et al*., *Nature* **496**, 196–200 (2013).
7. A. B. Khanikaev *et al*., *Nat. Mater.* **12**, 233–239 (2013).
8. J.-W. Dong, X.-D. Chen, H. Zhu, Y. Wang, X. Zhang, *Nat. Mater.* **16**, 298–302 (2017).
9. M. I. Shalaev, W. Walasik, A. Tsukernik, Y. Xu, N. M. Litchinitser, *Nat. Nanotechnol.* **14**, 31–34 (2019).
10. B. Yang *et al*., *Science* **359**, 1013–1016 (2018).
11. C. Poli, M. Bellec, U. Kuhl, F. Mortessagne, H. Schomerus, *Nat. Commun.* **6**, 6710 (2015).
12. P. St-Jean *et al*., *Nat. Photonics* **11**, 651–656 (2017).
13. B. Bahari *et al*., *Science* **358**, 636–640 (2017).
14. M. A. Bandres *et al*., *Science* **359**, eaar4005 (2018).
15. S. Klembt *et al*., *Nature* **562**, 552–556 (2018).
16. S. Barik *et al*., *Science* **359**, 666–668 (2018).
17. S. Mittal, E. A. Goldschmidt, M. Hafezi, *Nature* **561**, 502–506 (2018).
18. A. Blanco-Redondo, B. Bell, D. Oren, B. J. Eggleton, M. Segev, *Science* **362**, 568–571 (2018).
19. M. Jung, Z. Fan, G. Shvets, *Phys. Rev. Lett.* **121**, 086807 (2018).
20. D. Leykam, S. Mittal, M. Hafezi, Y. D. Chong, *Phys. Rev. Lett.* **121**, 023901 (2018).
21. Z. A. Kudyshev, A. V. Kildishev, A. Boltasseva, V. M. Shalaev, *Nanophotonics* **8**, 1349–1356 (2019).
22. M. I. Shalaev, W. Walasik, N. M. Litchinitser, *Optica* **6**, 839 (2019).
23. X. Cheng *et al*., *Nat. Mater.* **15**, 542–548 (2016).
24. L. Feng, R. El-Ganainy, L. Ge, *Nat. Photonics* **11**, 752–762 (2017).
25. B. Peng *et al*., *Nat. Phys.* **10**, 394–398 (2014).
26. J. Doppler *et al*., *Nature* **537**, 76–79 (2016).
27. D. Leykam, K. Y. Bliokh, C. Huang, Y. D. Chong, F. Nori, *Phys. Rev. Lett.* **118**, 040401 (2017).
28. K. Takata, M. Notomi, *Phys. Rev. Lett.* **121**, 213902 (2018).
29. H. Zhou *et al*., *Science* **359**, 1009–1012 (2018).
30. Materials, methods, and additional information are available as supplementary materials.

ACKNOWLEDGMENTS

Funding: We acknowledge the support from U.S. Army Research Office (ARO) (W911NF-19-1-0249) and the National Science Foundation (NSF) (ECCS-1846766 and CMMI-1635026). This research was partially supported by NSF through the University of Pennsylvania Materials Research Science and Engineering Center (MRSEC) (DMR-1720530). This work was carried out in part at the Singh Center for Nanotechnology, which is supported by the NSF National Nanotechnology Coordinated Infrastructure Program under grant NNCI-1542153. **Author contributions:** H.Z., L.F., and S.L. conceived the project. H.Z. conducted the design. H.Z., T.W., B.M., and S.L. constructed the theoretical model. X.Q. fabricated the samples. H.Z., T.W., X.Q., and L.F. performed the measurements and data analyses. L.F. guided the research. All authors contributed to manuscript preparation and discussion. **Competing interests:** The authors declare no competing interests. **Data and materials availability:** All data are available in the manuscript or the supplementary materials.

SUPPLEMENTARY MATERIALS

science.sciencemag.org/content/365/6458/1163/suppl/DC1
Supplementary Text
Figs. S1 to S9

20 May 2019; accepted 15 August 2019
10.1126/science.aay1064